ACS OMEGA

http://pubs.acs.org/journal/acsodf

Article

Defect-Engineered β-$MnO_{2-\delta}$ Precursors Control the Structure–Property Relationships in High-Voltage Spinel $LiMn_{1.5}Ni_{0.5}O_{4-\delta}$

Aderemi B. Haruna, Patrick Mwonga, Dean Barrett, Cristiane B. Rodella, Roy P. Forbes, Andrew Venter, Zeldah Sentsho, Philip J. Fletcher, Frank Marken, and Kenneth I. Ozoemena*

Cite This: *ACS Omega* 2021, 6, 25562–25573

Read Online

ACCESS | Metrics & More | Article Recommendations | Supporting Information

ABSTRACT: This study examines the role of defects in structure–property relationships in spinel $LiMn_{1.5}Ni_{0.5}O_4$ (LMNO) cathode materials, especially in terms of Mn^{3+} content, degree of disorder, and impurity phase, without the use of the traditional high-temperature annealing (≥700 °C used for making disordered LMNO). Two different phases of LMNO (i.e., highly $P4_332$-ordered and highly $Fd\bar{3}m$-disordered) have been prepared from two different β-$MnO_{2-\delta}$ precursors obtained from an argon-rich atmosphere (β-$MnO_{2-\delta}$ (Ar)) and a hydrogen-rich atmosphere [β-$MnO_{2-\delta}$ (H_2)]. The LMNO samples and their corresponding β-$MnO_{2-\delta}$ precursors are thoroughly characterized using different techniques including high-resolution transmission electron microscopy, field-emission scanning electron microscopy, Raman spectroscopy, powder neutron diffraction, X-ray photoelectron spectroscopy, synchrotron X-ray diffraction, X-ray absorption near-edge spectroscopy, and electrochemistry. LMNO from β-$MnO_{2-\delta}$ (H_2) exhibits higher defects (oxygen vacancy content) than the one from the β-$MnO_{2-\delta}$ (Ar). For the first time, defective β-$MnO_{2-\delta}$ has been adopted as precursors for LMNO cathode materials with controlled oxygen vacancy, disordered phase, Mn^{3+} content, and impurity contents without the need for conventional methods of doping with metal ions, high synthetic temperature, use of organic compounds, postannealing, microwave, or modification of the temperature-cooling profiles. The results show that the oxygen vacancy changes concurrently with the degree of disorder and Mn^{3+} content, and the best electrochemical performance is only obtained at 850 °C for LMNO-(Ar). The findings in this work present unique opportunities that allow the use of β-$MnO_{2-\delta}$ as viable precursors for manipulating the structure–property relationships in LMNO spinel materials for potential development of high-performance high-voltage lithium-ion batteries.

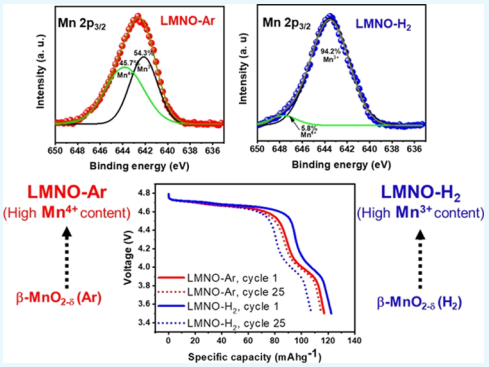

1. INTRODUCTION

The need for high-energy density lithium-ion batteries (LIBs) for plug-in hybrid electric vehicles, electric vehicles (EVs), and stationary storage applications continues to attract research interest for the development of high-voltage cathode materials. One such next-generation cathode material is the high-voltage spinel $LiMn_{1.5}Ni_{0.5}O_4$ (LMNO)[1−7] that is characterized by a higher working voltage (∼5.0 V) than commercialized materials (such as $LiCoO_2$, $LiFePO_4$, $LiNi_{1/3}Mn_{1/3}Co_{1/3}O_2$, and $LiMn_2O_4$).[8] The spinel LMNO has two possible crystal structures, being $Fd\bar{3}m$ and $P4_332$ symmetries.[9] The $Fd\bar{3}m$ symmetry has a face-centered cubic (FCC) structure with the Li positioned in the 8a site, while the Mn and Ni are randomly arranged in the 16d sites. Subsequently, the $Fd\bar{3}m$ symmetry is termed the disordered structure. The $P4_332$ symmetry has a primitive simple cubic structure with the Li positioned in the 8c sites, while the Mn and Ni are regularly arranged in the 12d sites and 4a sites, respectively. Hence, the $P4_332$ symmetry is known as the ordered structure. The disordered structure can be synthesized at temperatures well above 700 °C (e.g., 850 °C), while the ordered structure is synthesized at 700 °C.[10] Notwithstanding extensive research on spinel LMNO, the relationship between structural and the electrochemical properties is still an open theme.[9] The electrochemical properties of the spinel are among others related to the degree of disorder, doping, impurities, morphology, oxygen vacancy, and Mn^{3+} content. Since these are interrelated to the structural factors, the oxygen vacancy has been identified as a key contributing structural factor due to its correlation with the degree of disorder and Mn^{3+} content.[11]

It is common knowledge that oxygen-vacant, Mn^{3+}-rich LMNO exhibits improved electronic conductivity[12,13] and Li^+ transport for enhanced discharge capacity;[13] thus, the presence of Mn^{3+} in LMNO is a critical factor in the search for high-energy LMNO-based LIBs as energy is dependent on the

Received: July 11, 2021
Accepted: August 18, 2021
Published: September 22, 2021

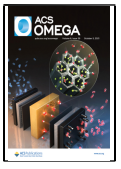

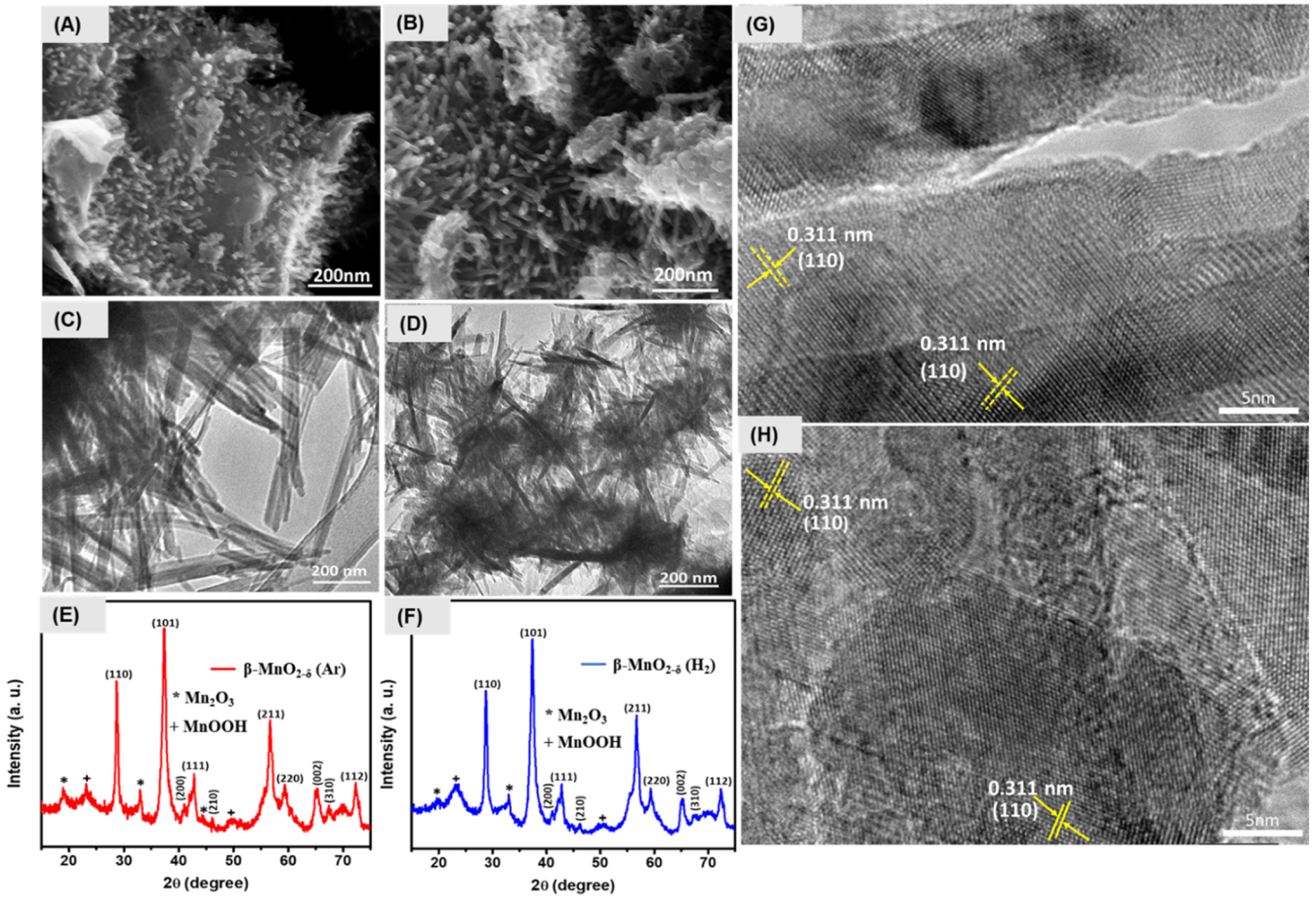

Figure 1. SEM images of (A) β-$MnO_{2-\delta}$ (Ar) and (B) β-$MnO_{2-\delta}$ (H_2). TEM images of (C) β-$MnO_{2-\delta}$ (Ar) and (D) β-$MnO_{2-\delta}$ (H_2). PXRD patterns of (E) β-$MnO_{2-\delta}$ (Ar) and (F) β-$MnO_{2-\delta}$ (H_2). HRTEM images of (G) β-$MnO_{2-\delta}$ (Ar) and (H) β-$MnO_{2-\delta}$ (H_2).

discharge capacity and voltage. However, Mn^{3+} has the drawback of a disproportionation reaction, which causes the dissolution of the Mn^{2+} into the electrolyte. The dissolved Mn^{2+} obstructs the diffusion of Li^+ during cycling and subsequently leads to capacity fading of the cell. Also, during cycling, the impurity phase in the disordered LMNO blocks the Li^+ mobility, thus reducing the cell capacity.[14] Therefore, the study of the relationship and control of these structural parameters is pertinent to the design, synthesis, and optimization of the spinel LMNO cathode materials for high-performing energy-dense LIBs.

In the search for improved LMNO materials, several workers have pursued different strategies. For example, Xiao et al.[15] used density functional theory (DFT) calculations and experimental investigations to establish that the oxygen vacancy in spinel LMNO changes directly with the degree of the disordered phase and Mn^{3+} content. On the other hand, Liu et al.[9] indicated that the oxygen vacancies that brought about the generation of Mn^{3+} and the impurity phase also induced Mn/Ni disorder. Therefore, these parameters are closely related. Furthermore, the authors[9] indicated that the doping of some transition metals into the spinel LMNO lattice can generate Mn^{3+} without the formation of oxygen vacancies, implying that the reduction process of Mn^{4+} to Mn^{3+} and the formation of oxygen vacancies in the spinel LMNO do not have a direct relationship. In advancing the argument, Xiao et al.[15] emphasized that although the presence of Mn^{3+} in the Cr-doped LMNO ($LiMn_{1.5}Ni_{0.45}Cr_{0.05}O_{4-\delta}$) is caused by the dopant, the oxygen vacancy also has its contributing effect to the Mn^{3+} content. These contentious findings clearly prove the need to study the structure−property relationship of these parameters on the electrochemical performance of the LIBs.[9,15]

In this research, the relationship between the structural parameters (oxygen vacancy, disordered phase, and Mn^{3+} and impurity contents) has been interrogated using two spinel LMNO materials having different oxygen vacancy contents, abbreviated herein as LMNO−Ar and LMNO−H_2. The β-$MnO_{2-\delta}$ nanorods [$MnO_{2-\delta}$ (Ar) and $MnO_{2-\delta}$ (H_2)] have been produced by a simple molten-salt process under different levels of reducing atmospheres. For the first time, these precursors have been used for the synthesis of oxygen-vacant spinels, LMNO−Ar and LMNO−H_2 cathode materials. These were done at both 700 and 850 °C without metal doping, the use of organic compounds and postannealing, the modification of the cooling profiles, or the use of microwave-assisted synthesis. Examination of the effects of oxygen vacancies on the electrochemical performance of the oxygen-vacant electrodes clearly reveals that the oxygen vacancies change concurrently with the degree of disorder and Mn^{3+}. Therefore, the strategic control of the oxygen vacancy in spinel LMNO via the use of low-cost and easy-to-prepare MnO_2 with different oxygen vacancies is thus proposed.

2. RESULTS AND DISCUSSION

2.1. Characterization of the β-$MnO_{2-\delta}$ Nanorods. The microstructure and the morphology of the β-$MnO_{2-\delta}$ were

https://doi.org/10.1021/acsomega.1c03656
ACS Omega 2021, 6, 25562−25573

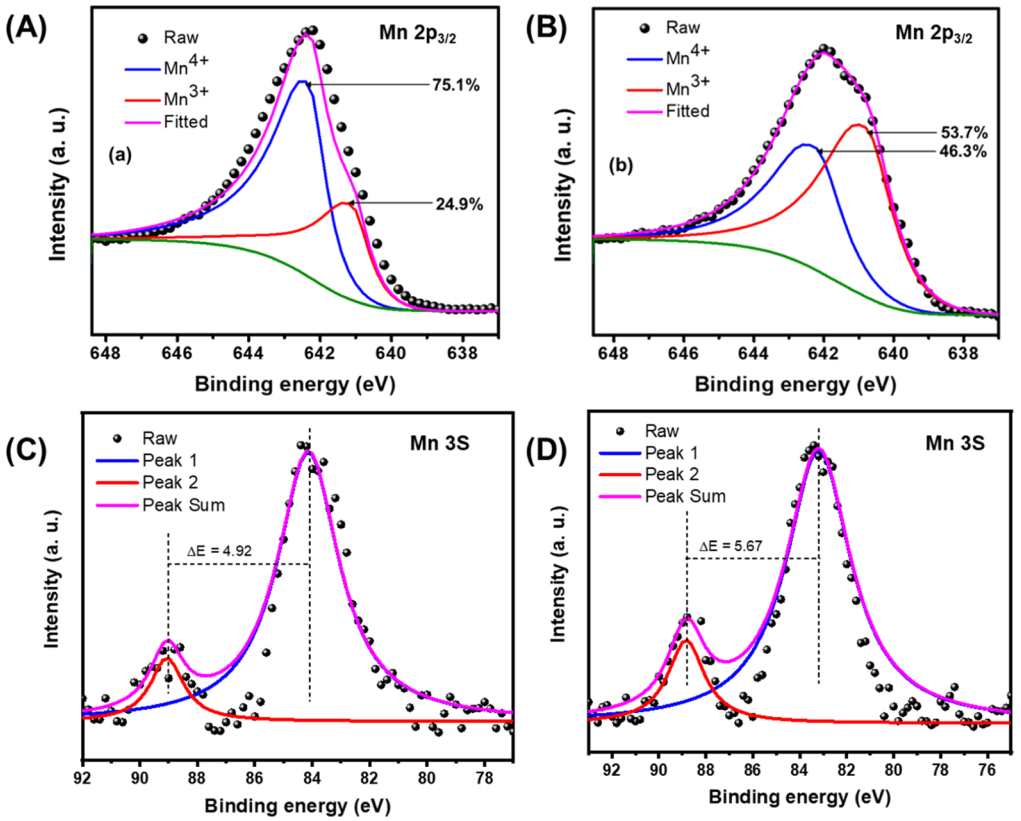

Figure 2. Mn $2p_{3/2}$ XPS spectra of (A) β-$MnO_{2-\delta}$ (Ar) and (B) β-$MnO_{2-\delta}$ (H_2) nanorods and Mn 3s XPS spectra of (C) β-$MnO_{2-\delta}$ (Ar) and (D) β-$MnO_{2-\delta}$ (H_2) nanorods.

Table 1. Data XPS Spectra

sample	Mn 3s				Mn $2P_{3/2}$				
	peak 1 (eV)	peak 2 (eV)	ΔE (eV)	valence	Mn^{3+} (eV)	Mn^{4+} (eV)	Mn^{3+} (%)	Mn^{4+} (%)	Mn^{3+}/Mn^{4+}
β-$MnO_{2-\delta}$ (Ar)	84.00	88.90	4.90	3.5	641.1	642.3	24.89	75.11	0.33
β-$MnO_{2-\delta}$ (H_2)	83.28	88.90	5.62	2.9	640.8	642.3	53.72	46.28	1.16

examined using X-ray diffraction (XRD), scanning electron microscopy (SEM), transmission electron microscopy (TEM), high-resolution TEM (HRTEM) and X-ray photoelectron spectroscopy (XPS). Figure 1A,B shows the SEM images for β-$MnO_{2-\delta}$–Ar and β-$MnO_{2-\delta}$–H_2 at 200 nm, respectively. The SEM images confirm the MnO_2 to be nanorods. Figure 1C,D shows the TEM images for β-$MnO_{2-\delta}$–Ar and β-$MnO_{2-\delta}$–H_2 at 200 nm, respectively. Both SEM and TEM images show that the two samples have similar nanorod-like shapes, and the SEM images look like free-standing nanorods with hollow spaces. The PXRD patterns of the MnO_2–Ar (Figure 1E) and MnO_2–H_2 (Figure 1F) taken with Cu Kα radiation exhibit strong (110), (101), and (211) peaks observed at 2θ = 28.7, 37.4, and 56.8°, respectively. The patterns are consistent with JCPDS card no. 24-0735 confirming MnO_2 being in the β-phase. The patterns also show weak peaks, attributed to the presence of MnOOH and Mn_3O_4 impurities.[16] The selected area electron diffraction (SAED) patterns of the two β-$MnO_{2-\delta}$ nanorods (Supporting Information, Figure S1), captured from a single nanorod of each, show the typical concentric circles that confirm polycrystalline morphology. The HRTEM images (Figure 1G,H) show that the interplanar spacing is 0.311 nm for β-$MnO_{2-\delta}$ (Ar) and β-$MnO_{2-\delta}$ (H_2). This is consistent with the (111) planes of β-MnO_2.

Figure 2A,B shows the Mn $2p_{3/2}$ XPS spectra of β-$MnO_{2-\delta}$ (Ar) and β-$MnO_{2-\delta}$ (H_2) nanorods, respectively, with the latter showing the higher Mn^{3+} content. Figure 2C,D shows the Mn 3s XPS spectra of β-$MnO_{2-\delta}$ (Ar) and (H) β-$MnO_{2-\delta}$ (H_2) samples. The Mn 3s spectra comprise a doublet of a high-spin state ($2p_{3/2}$) at the lower binding energy (peak 1) and low-spin state ($2p_{1/2}$) at the higher binding energy (peak 2). According to Wu et al.,[17] the separation between the two peaks (ΔE) is about 5.5 eV for Mn^{3+} and 4.5 eV for Mn^{4+}. The β-$MnO_{2-\delta}$ (H_2) has an increased value for ΔE (5.31 eV) compared to β-$MnO_{2-\delta}$ (Ar) (ΔE = 5.16 eV). The average Mn valences calculated from the conventional linear equation (V_{Mn} = 7.875 − 0.893 ΔE_{3s})[18] are 3.30 and 3.13 for the β-$MnO_{2-\delta}$ (Ar) and β-$MnO_{2-\delta}$ (H_2), respectively (Table 1). This result indicates that β-$MnO_{2-\delta}$ (H_2) has a higher Mn^{3+} content (thus higher surface oxygen vacancy) than the β-$MnO_{2-\delta}$ (Ar).[16,19,20] This corroborates the Mn $2p_{3/2}$ spectral data.

For charge neutrality, MnO_2 contains only Mn^{4+}. The presence of Mn^{3+} in the two precursor MnO_2 materials is due to the partial reduction of the Mn^{4+} to compensate for oxygen loss during the synthesis in Ar/H_2 and H_2 environments for the β-$MnO_{2-\delta}$ (Ar) and β-$MnO_{2-\delta}$ (H_2) nanorods, respectively. Thus, this confirms the introduction of oxygen defects (vacancies) into the two samples. It is of interest to note that

https://doi.org/10.1021/acsomega.1c03656
ACS Omega 2021, 6, 25562−25573

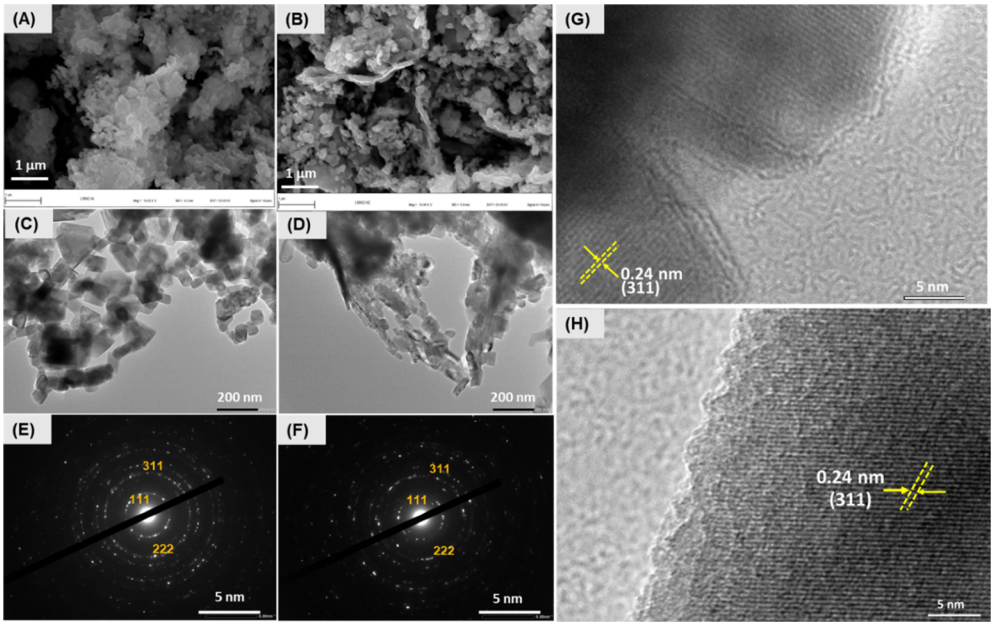

Figure 3. SEM images (A) of LMNO−Ar and (B) of LMNO−H_2, HRTEM images of (C,G) LMNO−Ar and (D,H) LMNO−H_2, and SAED patterns of (E) LMNO−Ar and (F) LMNO−H_2.

Figure 2A,B shows that the percentage of Mn^{3+} in β-$MnO_{2-\delta}$ (H_2) spectra (53.7%) (Figure 2B) is significantly higher than that of -$MnO_{2-\delta}$ (Ar) (24.9%) (Figure 2A). This is because β-$MnO_{2-\delta}$ (H_2) was synthesized under an extremely reducing (H_2) environment relative to the less-reducing atmosphere used for the β-$MnO_{2-\delta}$ (Ar). Consequently, the higher Mn^{3+} peak intensity and area of β-$MnO_{2-\delta}$ (H_2) spectra confirm its higher oxygen vacancy content than that of the β-$MnO_{2-\delta}$ (Ar).

2.2. Characterization of the LMNO Samples Obtained from the β-$MnO_{2-\delta}$ Nanorods. Insights into the physicochemical properties of the LMNO samples have been provided using several techniques, including SEM, TEM, HRTEM, synchrotron XRD (SXRD), synchrotron XPS, powder neutron diffraction (PND), Brunauer−Emmett−Teller (BET), thermogravimetric analysis (TGA), and Fourier-transform infrared spectroscopy (FTIR). Figure 3A,B depicts typical SEM images of LMNO−Ar and LMNO−H_2, respectively. Both samples generally show mostly cubic morphology and some nanorods (Supporting Information, Figure S2) with particles sizes in the range 50−150 nm. The corresponding HRTEM images (Figure 3C,D) show that some of the particles are rod-like. As evident from the SAED patterns (Figure 3E,F), the two LMNO materials are highly crystalline. Also, the HRTEM images (Figure 3G,H) of the two LMNO samples have interplanar spacings of ∼0.24 nm which is consistent with the characteristic (311) plane of the fcc crystal structures.

For the BET surface area, the LMNO−H_2 sample has higher values, pore size and volume, than the LMNO−Ar sample, as shown in Table 2. The higher surface area of the LMNO−H_2 sample promises to offer a larger area for Li^+ extraction and insertion which enhances the conductivity (capacity) of the electrode in the charge−discharge processes. The higher surface area in LMNO−H_2 correspondingly offers a larger electrode−electrolyte surface contacts which increases the side reactions at the interface and thus causes the LMNO−H_2 cathode material to degrade faster during cycling. These observations are expected to be reflected in the charge−discharge performances of the LMNO−Ar and LMNO−H_2 electrodes during cycling. The TGA profiles for the LMNO−Ar and LMNO−H_2 samples (Supporting Information, Figure S3) show that the LMNO−H_2 lost about 1.5% of its weight before 300 °C, while LMNO−Ar only lost about 0.4% under the same conditions (details in Supporting Information).

Table 2. Nitrogen Adsorption−Desportion (BET) Data and Rietveld Refinement Obtained from SXRD and PND Data for the LMNO−Ar and LMNO−H_2 Samples Obtained at 700 °C

Parameters	LMNO−Ar	LMNO−H_2	% difference
surface area (m^2 g^{-1})[a]	7.0	7.9	12.9
pore volume (cm^3g^{-1})[a]	0.108	0.132	22.2
pore size (nm)[a]	60.1	67.0	11.5
phase $P4_332$ content (%)[b]	86.2	94.1	
phase $Fd\bar{3}m$ content (%)[b]	0.10	5.9	
rock salt ($Li_{0.8}Mn_{0.81}O_2$) content (%)[b]	13.7		
NiO impurity (%)[c]	11.8	0.1	

[a]Nitrogen adsorption−desoprtion (BET) data. [b]SXRD Reitveld refinement. [c]PND Reitveld refinement.

The SXRD patterns of LMNO−Ar and LMNO−H_2 samples are presented in Figure 4A,B. The two samples show strong diffraction peaks, depicting high crystallinity. The two samples have the (111) peak positioned at about 18.8° and other peaks at their respective position in correlation to the model spinel LMNO structure. Furthermore, the SXRD patterns of the two samples do not show the superlattice peaks (2θ = 15.4, 39.8, 45.8, and 57.6°) which is synonymous to $P4_332$. Hence, the LMNO−Ar and LMNO−H_2 samples can be indexed to $Fd\bar{3}m$ symmetry.[21] However, the superlattice peaks may have been too weak for the synchrotron X-ray powder diffraction analytical technique to detect.[22]

Unlike the LMNO−H_2, the diffraction pattern of LMNO−Ar shows the presence of a secondary (rock salt) phase,

https://doi.org/10.1021/acsomega.1c03656
ACS Omega 2021, 6, 25562−25573

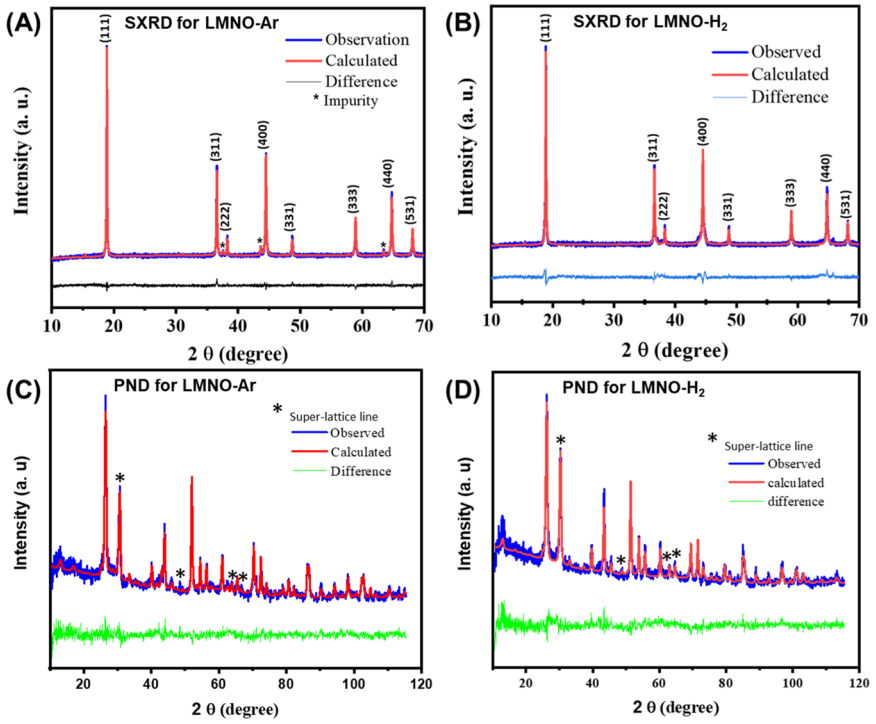

Figure 4. SXRD patterns of (A) LMNO−Ar and (B) LMNO−H_2 and PND patterns of (C) LMNO−Ar and (D) LMNO−H_2.

identified by the Rietveld refinement as rhombohedral layered rock salt ($Li_{0.8}Mn_{0.81}O_2$) of 13.7 wt %, as well as the NiO phase (11.8%) in the diffraction patterns (Table 2). This observation is of great interest because it suggests that the experimental atmospheres used in this research work can be used to control the impurity phases in spinel LMNO. Ke et al.[14] reported that the impurity phase in spinel LMNO hinders the mobility of Li^+ in the cathode material, thereby lowering the cell capacity. Consequently, the LMNO−Ar sample with a higher amount of impurity is expected to have a lower capacity than the LMNO−H_2 sample (and this will be shown later).

In the classical spinel LMNO structure, the XRD (111) Miller index has the highest intensity, while the (311) Miller index has the highest in the antispinel structure.[21] It can be inferred that the LMNO−Ar and LMNO−H_2 have spinel structures. The XRD peak intensity ratio, I_{111}/I_{311}, is a suitable indicator to differentiate between the disordered and ordered phases.[23] The I_{111}/I_{311} values for LMNO−Ar and LMNO−H_2 are 1.9959 and 2.0650, respectively. The I_{111}/I_{311} values of the model disordered phase (JCPDS: 32-0581) and ordered phase (JCPDS: 80-2184) are 1.67 and 2.61, respectively. It can be inferred that the two samples (LMNO−Ar and LMNO−H_2) have disordered and ordered phases because their I_{111}/I_{311} values are in between that of the JCPDS values. The I_{111}/I_{311} value relates to the degree of confusion among the Li^+ and transition-metal ions in LMNO. Furthermore, the I_{111}/I_{311} value is inversely proportional to the degree of confusion and the degree of confusion relates inversely to Li transport (conductivity).[21] The LMNO−H_2 sample exhibits a slightly higher I_{111}/I_{311} value (2.0650) than the LMNO−Ar sample (1.9959), suggesting that the LMNO−H_2 sample may have a lower degree of confusion relative to the LMNO−Ar sample. Consequently, the LMNO−H_2 sample should show a smoother path for Li^+ transport and thus better conductivity. The structural stability of spinel LMNO increases with the increase in the I_{311}/I_{400} value.[24] The I_{311}/I_{400} value is slightly higher for LMNO−Ar (0.9117) than that for the LMNO−H_2 (0.8999), suggesting that LMNO−Ar should exhibit higher structural stability than LMNO−H_2, and the cycle performance of LMNO−Ar is expected to be better than LMNO−H_2 (as observed and will be discussed in the next section on electrochemistry).

Figure 4C,D shows the PND patterns of the LMNO−Ar and LMNO−H_2. The diffraction pattern of the LMNO−H_2 sample shows peak shift toward the lower angles. This is consistent with the expansion of the unit cell.[25] The PND Rietveld refinement showed that the lattice parameter of LMNO−H_2 (8.27246 Å) is larger than the lattice parameter of LMNO−Ar (8.18073 Å). The increased lattice parameter of LMNO−H_2 can be related to the increase in its Mn^{3+} content since the Mn^{3+} ionic radius (0.65 Å) is higher than that of Mn^{4+} (0.54 Å).[21] This subsequently leads to a larger cell volume of 566.11 $Å^3$ in LMNO−H_2 than that of 547.49 $Å^3$ LMNO−Ar. It is expected to offer larger Li^+ pathways and thus higher electronic and ionic conductivity than in LMNO−Ar (as observed and will be discussed in the next section on electrochemistry). Furthermore, the superstructure lines are observed in the two samples' powder neutron diffraction patterns which confirm that the presence of $P4_332$ phases.[26] This is consistent with the SXRD Reitveld refinement results (Table 2).

Figure 5A,B shows the deconvoluted Mn $2p_{3/2}$ XPS spectra of LMNO−Ar and LMNO−H_2 cathode materials. Table 3 displays values obtained from the fitted peaks. The Mn $2p_{3/2}$ XPS binding energy of Mn^{3+} on the surface of LMNO−Ar and LMNO−H_2 samples are positioned at 642.1 and 643.5 eV, respectively, while the Mn $2p_{3/2}$ XPS binding energy of Mn^{4+} on the surface of LMNO−Ar and LMNO−H_2 cathode is positioned at 643.8 and 645.9 eV, respectively. A positive shift of the binding energy is well-known to be related to reduced electron density around the base element. Thus, the significant shift in the binding energy of the LMNO−H_2 is indicative of the reduced electron density (due to oxygen vacancies) around

https://doi.org/10.1021/acsomega.1c03656
ACS Omega 2021, 6, 25562−25573

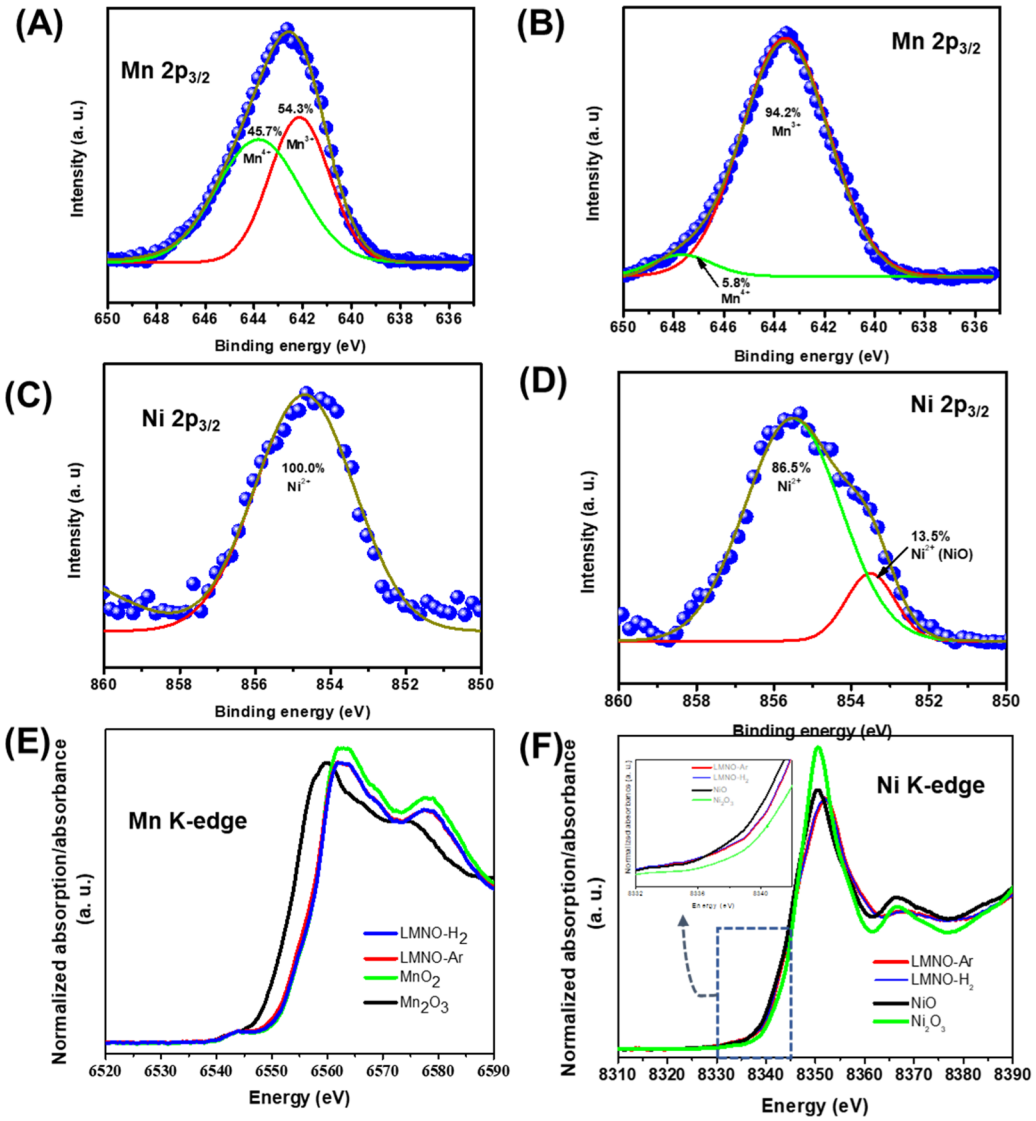

Figure 5. Mn $2p_{3/2}$ XPS spectra of (A) LMNO−Ar and (B) LMNO−H_2; Ni $2p_{3/2}$ XPS spectra of (C) LMNO−Ar and (D) LMNO−H_2; and (E) Mn K-edge XANES and (F) Ni K-edge XANES (inset in Figure 5F shows edge shift between NiO and Ni_2O_3 spectra).

Table 3. XPS Analysis Results: LMNO−Ar and LMNO−H_2 Cathode Materials

	binding energy (eV)		%		binding energy (eV)			%	
Sample	Mn^{3+}	Mn^{4+}	Mn^{3+}	Mn^{4+}	Ni^{2+} (NiO)	Ni^{2+} (NiO)	Ni^{2+} ($Ni(OH)_2$)	Ni^{2+} (NiO)	Ni^{2+} ($Ni(OH)_2$)
LMNO−Ar	642.1	643.8	46.4	53.6		854.7		100	
LMNO−H_2	643.5	645.9	86.8	13.2	853.7		855.5	13.5	86.5

the Mn. Similar binding energies have been reported by Nesbitt and Banerjee.[27] The LMNO−H_2 cathode material's Mn^{3+} content (86.8%) is greater than that of the LMNO−Ar (46.4%).

The results further confirm the presence of Mn^{3+} (disordered phase) and Mn^{4+} (ordered phase) on the surface of the two samples, and the Mn^{3+} content on the surface of LMNO−H_2 is more than that on the surface of LMNO−Ar. The presence of Mn^{3+} in the XPS spectra of LMNO−Ar and LMNO−H_2 can be attributed to the generation of an oxygen vacancy and higher percentage of Mn^{3+} in LMNO−H_2 which can be ascribed to a higher concentration of oxygen vacancy. This result agrees with the results of the SXRD, Raman spectroscopy, X-ray absorption near-edge spectroscopy (XANES), and GCV. Figure 5C,D and Table 3 show the fitted Ni $2p_{3/2}$ XPS spectra and data analysis of LMNO−Ar and LMNO−H_2 cathode materials. The fitted spectrum of LMNO−Ar has only one peak situated at a binding energy of 854.7 eV. This peak can be allotted to Ni^{2+} as the value is similar to 854.8 eV.[28] The LMNO−H_2-fitted spectrum showed two peaks which are positioned at 853.7 and 855.5 eV. The binding energy at 853.7 eV is due to Ni $2P_{3/2}$ (Ni^{2+} or NiO).[29,30] The binding energy at 855.5 eV is assigned to Ni^{3+} (855.6 eV)[28,31] or Ni^{2+} [$Ni(OH)_2$] (855.5 eV).[15,32] FTIR confirmed the presence of the OH bond in the LMNO−H_2 sample (see Supporting Information, Figure S3). Raman spectroscopy is a sensitive technique to probe the local environments of spinel LMNO. Raman spectra (Figure S4)

https://doi.org/10.1021/acsomega.1c03656
ACS Omega 2021, 6, 25562−25573

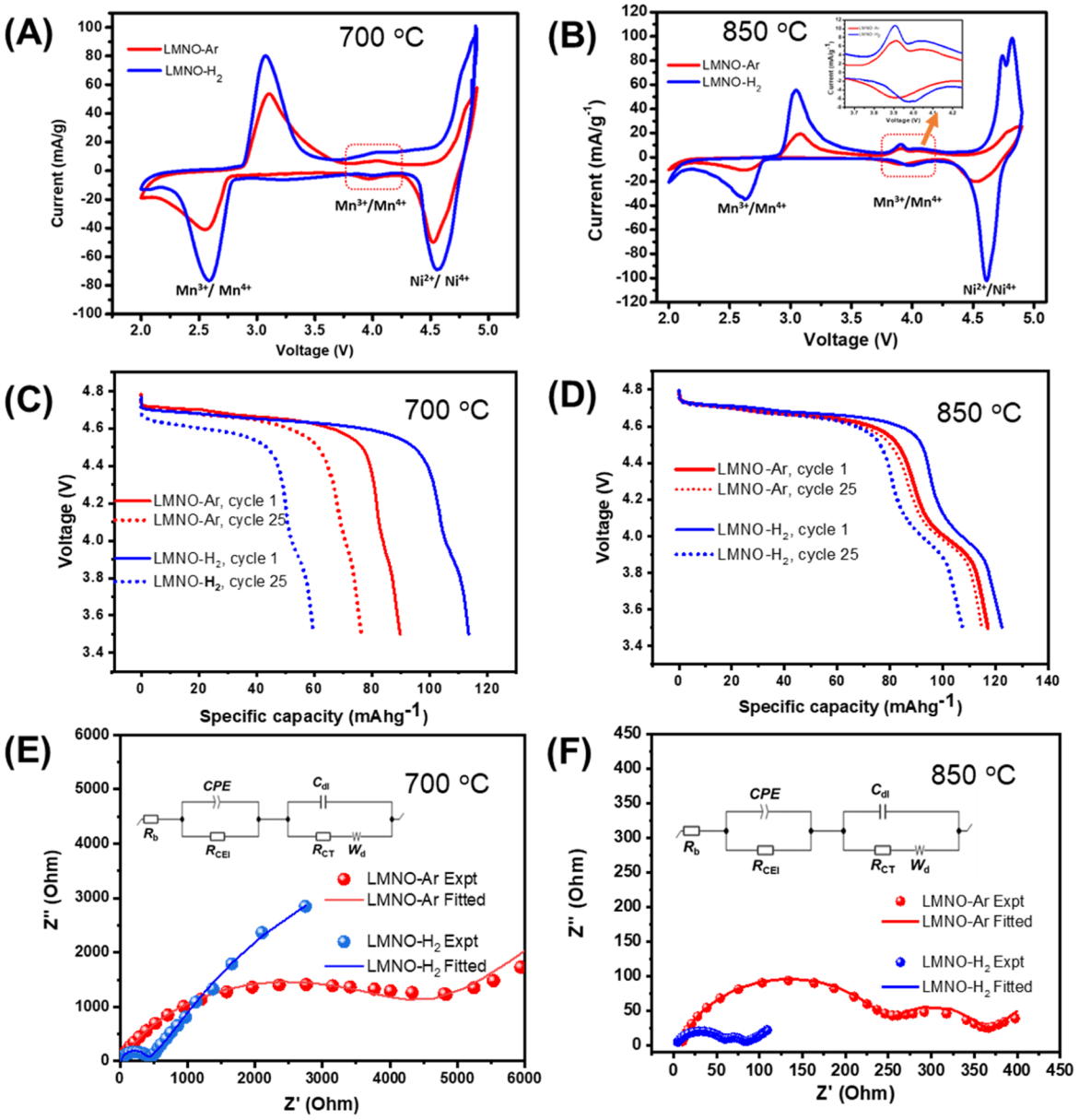

Figure 6. Cyclic voltammograms of LMNO−Ar and LMNO−H_2 at 0.1 mV s^{-1} for samples obtained at (A) 700 and (B) 850 °C; discharge capacity of LMNO−Ar and LMNO−H_2 at a 0.1 C rate (inset, broken rectangle) for samples obtained at (C) 700 and (D) 850 °C; and Nyquist plots of LMNO−Ar and LMNO−H_2 obtained prior to cycling at OCV (4.7 V) for samples obtained at (E) 700 and (F) 850 °C.

show that the LMNO−H_2 sample has a higher degree of disordered phase than LMNO−Ar, (details in the Supporting Information). The XANES result showed that the Ni exists as Ni^{2+} in LMNO−H_2. Furthermore, as will be shown in the next section on electrochemistry, the cyclic voltammogram of LMNO−H_2 has only one peak at 4.7 V, confirming the presence of Ni^{2+} only.[13] Consequently, the binding energy 855.5 eV can be ascribed to Ni^{2+} ($Ni(OH)_2$) and not Ni^{3+}. This finding also proves that LMNO−H_2 has a higher oxygen vacancy.

The oxidation states of Mn and Ni in the LMNO−Ar and LMNO−H_2 samples were examined by XANES. Figure 5E shows that the Mn K-edge spectra of the two samples are similar. The Mn K-edge spectra of LMNO−Ar and LMNO−H_2 samples are positioned within that of the Mn^{3+} and Mn^{4+} standards. This result confirms the co-existence of the two phases, that is, Mn^{3+} (disordered) and Mn^{4+} (ordered) in the LMNO−Ar and LMNO−H_2 samples. The Mn oxidation state is thus between +3 and +4. Figure 5F shows the Ni K-edge spectra of the two samples and the Ni standards [NiO (Ni^{2+}) and Ni_2O_3 (Ni^{3+})], with a clear edge shift between NiO and Ni_2O_3 spectra (see Figure 5F inset). The spectra of the two samples are similar and very close to that of the Ni^{2+} and no significant change in the spectra of the LMNO−Ar and LMNO−H_2 samples. This result confirms that the Ni in the two samples exists as Ni^{2+}. The Mn and Ni K edge of the samples' spectra have weak pre-edge regions.

2.3. Electrochemical Measurements. Electrochemical properties were investigated using cyclic voltammetry (current *vs* voltage: CV), galvanostatic charge−discharge (GCD), and electrochemical impedance spectroscopy (EIS). The cyclic voltammograms of the LMNO−Ar and LMNO−H_2 electrodes at 0.1 mV s^{-1} reveal the signature redox couples of LMNO (Figure 6A,B). The CV curves are very similar and consist of

https://doi.org/10.1021/acsomega.1c03656
ACS Omega 2021, 6, 25562−25573

Table 4. EIS Parameters for the LMNO-Based Cells with LMNO Samples Obtained at Both 700 and 850 °C Annealing Temperatures

EIS parameters	electrode materials			
	@700 °C		@850 °C	
	LMNO−Ar	LMNO−H_2	LMNO−Ar	LMNO−H_2
R_b/Ω	22.10 ± 0.28	23.10 ± 0.36	8.46 ± 0.44	2.73 ± 1.26
R_{CEI}/Ω	34.10 ± 11.15	2825.00 ± 33.27	248.5 ± 1.982	58.49 ± 3.31
CPE/μF $s^{(a-1)}$	0.008 ± 0.00	9.50 ± 0.36	14.99 ± 1.11	28.25 ± 16.47
A	0.71	0.96	0.83	0.79
C_{dl}/mF	0.80 ± 0.20	0.30 ± 0.00	1.023 ± 0.06	1.347 ± 0.45
R_{CT}/Ω	4153 ± 29.11	353.90 ± 0.77	96.26 ± 0.91	20.60 ± 2.93
Z_d/Ω $s^{-}0.5$	1900 ± 0.22	383.7 ± 2.02	14.07 ± 0.19	6.00 ± 0.13

three redox peaks in the regions 2.5−3.0 V, around 4 V, and 4.5−4.9 V. The strong redox couple at the lower voltages (anodic peak ∼3.1 V and cathodic peak ∼2.6 V) is due to the Mn^{3+}/Mn^{4+} redox reactions.[33] The small peak around 4.0 V also signifies the Mn^{3+}/Mn^{4+} redox reactions. The presence of Mn^{3+} reveals that the two samples have some degree of the disordered phase, being higher in LMNO−H_2, corroborating the results of the analytical techniques in the previous sections. Given that the Mn^{3+} content changes directly with the degree of disorder[15] implies that the LMNO−H_2 cathode material has a higher degree of disorder than the LMNO−Ar. The higher degree of the disorder phase is expected to have better electronic and Li^+ conductivity because of its higher Mn^{3+} content and thus higher specific capacity. Figure 6C shows the discharge capacity profiles of LMNO−Ar and LMNO−H_2 cathode materials at a 0.1 C rate, between the 1st and 25th cycles: LMNO−H_2 has a value of 113.6 mA h g^{-1} and decays to 59.6 mA h g^{-1} after 25 cycles (retention capacity of 52.7%); LMNO−Ar has a value of 90.1 mA h g^{-1} and decays to 76.3 mA h g^{-1} after 25 cycles (capacity retention: 84.7%). Although the specific capacity is lower than the theoretical value (∼147 mA h/g), it is interesting to note that even at low annealing temperature (700 °C), the obtained specific capacity is in the range reported by others such as Nisar et al.,[34] Wu et al.,[35] and who reported 106 and 121 mA h/g for LMNO, respectively. However, the LMNO obtained at higher annealing temperature (850 °C) showed higher and more stable capacity (Figure 6D) than the samples obtained at 700 °C (Figure 6C).

The voltage plateau around 4 V can be used to estimate the relative amount of Mn^{3+} in spinel LMNO. From Figure 6A,B (broken rectangle), a voltage plateau occurred around 4 V for the LMNO−H_2 which is larger than that seen in the LMNO−Ar, clearly suggesting that the Mn^{3+} content of LMNO−H_2 is higher than that of LMNO−Ar. In both cases (i.e., at 700 and 850 °C, Figure 6C,D), the LMNO−Ar showed better cycling stability than the LMNO−H_2 counterpart.

The reason lies in the knowledge that the LMNO−H_2 cathode material with high Mn^{3+} content should be more prone to the disproportionation reaction (hence higher capacity fading) than the LMNO−Ar with low Mn^{3+} content. The electrochemistry of LMNO−Ar and LMNO−H_2 cathode, which proves the co-existence of disordered and ordered phases, is consistent with the PXRD, Raman, and XANES data. The high specific discharge capacity shown by the LMNO−H_2 cathode material may be attributed to the following reasons: (i) higher degree of oxygen vacancy; (ii) higher degree of disordered phase; (iii) higher Mn^{3+} content (more conducting); (iv) lower impurity content; (v) higher BET surface area data; and (vi) lower extent of confusion between Li^+ and transition cations. The higher Mn^{3+} content in the LMNO−H_2 electrode will lead to a higher amount of soluble Mn^{2+} in the electrolyte by the disproportionate reaction, hence the poorer stability or capacity fading upon repetitive cycling (see also Figure S5B). On the other hand, the LMNO−Ar cathode material exhibits low specific capacity but higher cycling stability because of its lower Mn^{3+} content (higher Mn^{4+}) and higher impurity contents; impurities are known to restrict the Li^+ mobility. The lower BET surface area of the LMNO−Ar cathode material offered a reduced surface contact with the electrolyte, thus reduction in the side reactions and consequently a higher retention capacity. Both electrodes show essentially similar Coulombic efficiency (Figure S5) of ∼97%, in agreement with the literature.[36]

Next, EIS measurements were used to provide some insights into the all-important interfacial electrochemistry,[37−46] including the ease at which electrons and Li ions move across the electrode−electrolyte interface. The Nyquist plots for the two electrodes (Figure 6E,F), show intercept in the high-frequency area of the real impedance (Z') axis, a semicircle in the middle-frequency area, and a sloping line in the lower-frequency area. The Nyquist plots were satisfactorily fitted with the conventional lithium-ion battery electrical equivalent circuit,[46] that is, combination of an RC and a Randles circuit (Figure 6E,F inset) made up of the following parameters: the bulk resistance (R_b) of the battery cell (due to the series connection of the electrode, current collectors, electrolyte, and separator); constant phase element (CPE) due to the capacitance of the interfacial layer which is affected by the inhomogeneity of the electrode surface, cathode−electrolyte interfacial resistance (R_{CEI}), double-layer capacitance (C), charge-transfer resistance (R_{CT}) due to electronic transport, and Warburg impedance (W_d) due to Li-ion diffusion. As seen in Table 4, the overall resistance (R_b + R_{CEI} + R_{ct}) values decrease as follows: LMNO−Ar at 700 °C (4209 Ω) > LMNO−H_2 at 700 °C (3202 Ω) ≫ LMNO−Ar at 850 °C (353 Ω) ≫ LMNO−H_2 at 850 °C (82 Ω).

The results show that at both annealing temperatures investigated, the LMNO−H_2 gives the best electrical conductivity compared to the LMNO−Ar counterpart, confirming the higher Mn^{3+} content of the former than the latter. The EIS results are consistent with the physicochemical data described already.

Finally, DFT calculations were used to interrogate the effects of oxygen vacancy on the conductivity of the LMNO cathode materials. These show (Figure S6) that the band gap decreases as oxygen is removed from the supercell: LMNO phase ($LiMn_{1.5}Ni_{0.5}O_4$, $P4_332$ = 4.604 eV) > ($LiMn_{1.5}Ni_{0.5}O_{4-\delta}$, $Fd\bar{3}m$ = 4.597 eV) > ($LiMn_{1.5}Ni_{0.5}O_{4-2\delta}$, $Fd\bar{3}m$ = 4.547 eV),

https://doi.org/10.1021/acsomega.1c03656
ACS Omega 2021, 6, 25562−25573

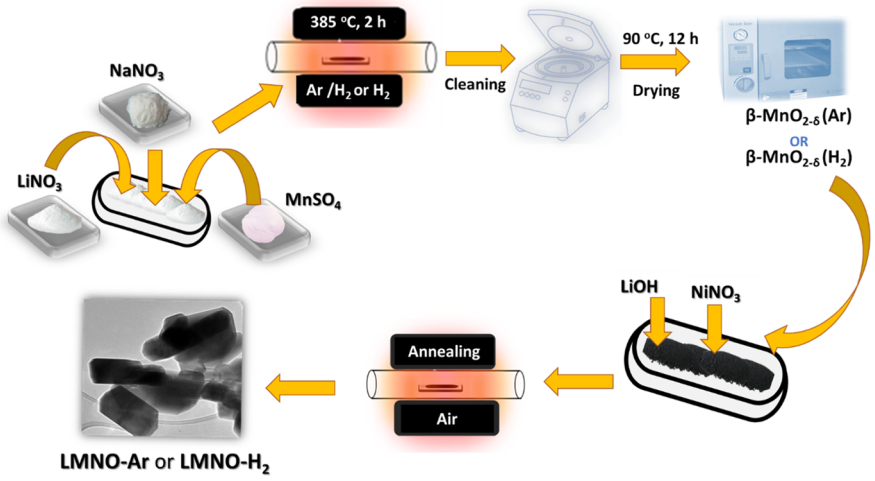

Figure 7. Schematic representation of the preparation of defect-engineered β-$MnO_{2-\delta}$ nanorods and their corresponding $LiMn_{1.5}Ni_{0.5}O_{2-\delta}$ cathode materials.

clearly confirming that the conductivity of LMNO increases with the increase in oxygen vacancy.

3. CONCLUSIONS

Oxygen vacancies in LMNO−Ar and LMNO−H_2 were successfully synthesized by controlling the precursors' (β-$MnO_{2-\delta}$) synthesis atmosphere. The different levels of reducing atmospheres under which the precursors were synthesized are identified as the key factors for the introduction of the oxygen vacancies into the LMNO−Ar and LMNO−H_2 cathode materials. The CV and GCD results confirmed the co-existence of disordered and ordered phases in the LMNO−Ar and LMNO−H_2 samples with different Mn^{3+} contents. The higher discharge capacity of the LMNO−H_2 sample relative to that of the LMNO−Ar is attributed to its higher degree of oxygen vacancies, disorder, Mn^{3+} content, and lower impurities. The more severe capacity fading of the LMNO−H_2 sample is also ascribed to the same trend of indices (oxygen vacancies, disorder, Mn^{3+} content, and impurities). In addition, the high-oxygen vacancy LMNO−H_2 sample cathode material has a high R_{CEI} which caused significant change to the electrochemical properties of the LIB. Thus, we can infer that the careful control of the synthetic atmosphere of the precursors is critical to have appropriate contents of oxygen vacancies, disorder, Mn^{3+} content, impurities, and CEI for the improved electrochemical performance of spinel LMNO. The oxygen vacancy content in the spinel LMNO cathode material changes concurrently with the Mn^{3+} content and degree of disorder but not with the impurity content. Therefore, it can be proposed that these fundamental findings can be valuable contributors to the design, synthesis, and optimization of improved spinel LMNO for LIBs.

4. EXPERIMENTAL SECTION

4.1. Synthesis of $MnO_{2-\delta}$ (Ar) and $MnO_{2-\delta}$ (H_2) Nanorods. The precursors, $MnO_{2-\delta}$ (Ar) and $MnO_{2-\delta}$ (H_2) nanorods, were synthesized using the modified molten salt method.[16,47] Weight ratio 1:5:10 of the $MnSO_4$, $LiNO_3$, and $NaNO_3$ was, respectively, grounded using a mortar and pestle. The mix was heated in a tube furnace at 385 °C (2.0 h) under an argon (5%)/hydrogen (95%) atmosphere to obtain the precursor, β-$MnO_{2-\delta}$ (Ar) nanorods, and hydrogen (100%) atmosphere to obtain the precursor: β-$MnO_{2-\delta}$ (H_2) nanorods. The two products were allowed to cool naturally under their respective prevailing atmospheres. The samples were washed several times with distilled water and dilute H_2SO_4 acid and dried at 90 °C overnight.

4.2. Synthesis of LMNO Nanorods (LMNO−Ar and LMNO−H_2). The LMNO nanorods were synthesized by the modified solid-state reaction.[48] The molar ratio of 1.5:0.5:1.05 of β-$MnO_{2-\delta}$ (H_2) nanorods, $Ni(NO_3)_2{\cdot}6H_2O$, and LiOH was dispersed in ultrapure water. It was then mixed in a magnetic stirrer and dried in an oven at 80 °C. The dried sample was hereafter heated in air at 700 or 850 °C for 18 h to obtain the product LMNO−H_2. The synthesis of the LMNO−Ar followed the same procedure except for the precursor [β-$MnO_{2-\delta}$ (Ar)] nanorods that were used (schematically illustrated in Figure 7).

4.3. Physicochemical Characterization. Powder XRD patterns were obtained at the D10-B, XPD beamline at the LNLS synchrotron (Brazil) to provide data good for refinement because of the extremely high signal/noise ratio of the diffraction pattern.[49] A photon energy of 8.0 keV was used with data collected using a linear detector (Mythen 1 K). The crystalline phase identification was performed using DIFFRAC.EVA (Version 2. Release 2014) in conjunction with the ICDD PDF2 database (Release 2016). Phase quantification was performed using the Rietveld method as implemented in Bruker AXS TOPAS software (Version 5, 2014). PND analysis was performed at the SAFARI-1 research reactor at the South African Nuclear Energy Corporation SOC Limited (NECSA). The high-performance neutron diffraction instrument, Powder Instrument for Transition in Structure Investigations (PITSI),[50] was used to obtain data at room temperature using a wavelength of 1.08 Å and a 4 position-sample changer that continuously rotated the samples. The diffraction patterns were measured by 17° step scans of the area detector bank to cover 10−115° in 2θ. The samples were contained in thin-walled vanadium tubes and fully illuminated using an incident beam size of 5 × 35 mm^2. Data acquisition times ranged from 4 to 10 h to get good statistics. Refinements were carried out with GSAS II. XPS measurements were performed at the LNLS Synchrotron (Brazil) using an electron analyzer SPECS, model Phoibos HAS-3500 150, with a monochromatic Al Kα ($h\nu$ = 1486.61 eV). The mono-

https://doi.org/10.1021/acsomega.1c03656
ACS Omega 2021, 6, 25562−25573

chromatic Al Kα source was operated at 10 kV and 10 mA and the spectra were obtained with an analyzer pass energy of 20 eV. The samples in the powder form were supported on double-sided carbon tape and fixed on the XPS sample holder. The spectra were analyzed using the software CasaXPS, version 2.2.99. The spectra were analyzed using the software CasaXPS, version 2.2.99. XANES analysis at the Mn K-edge (8333 eV) and Ni K-edge (6539 eV) was performed at the D06A-DXAS beamline of the LNLS. DXAS is a dispersive beamline equipped with a focusing curved Si(111) monochromator, operating in the Bragg mode, that selects the X-ray energy bandwidth (11 400−12 000 eV), with a 1152 × 1242 (500 × 900) pixel CCD solid-state detector that converts X-rays into visible light for spectral analysis. The monochromator was calibrated with Ni and Mn foils prior to each measurement. Extraction of the XANES signal was carried out using the Demeter software package.[51] BIOVIA Materials Studio DMol3 module was used to carry out the DFT calculations. A supercell of 3 × 3 × 3 (448 atoms) for $Li_2Mn_3NiO_8$ was modeled and its geometry was optimized. An accuracy threshold was set as 10^{-6} eV and Perdew−Wang generalized gradient approximation (PW91) functionals employed. The 514.5 nm line of an argon-ion laser and a Horiba Jobin-Yvon LabRAM HR Raman spectrometer equipped with an Olympus BX41 microscope attachment was used to obtain the Raman studies. The LabSpec v5 software was used to capture the data. The FTIR spectra were recorded using a Thermo Nicolet 6700 FTIR spectrometer. The TEM images of the samples were captured using an FEI Tecnai T12 Sprint instrument (at Wits) and TEM, JEOL JEM-2100Plus (at University of Bath). The surface area of the samples was determined by the Micrometric Tristar 3000 BET. The SEM images were captured using the FEI Nova Nanolab 600 Instrument. XPS spectra were collected with a Thermo ESCAlab 250Xi spectrometer. TGA was carried out using a TGA 4000: PerkinElmer between 35 and 900 °C at a heating rate of 5 °C min^{-1} in an air gas rate of 20 mL/min and a nitrogen gas rate of 20 mL/min. The electrochemistry of LMO samples obtained at 700 and 850 °C shows similar activity trends in terms of oxygen vacancies (e.g., Mn^{3+} content in LMNO−H_2 > LMNO−Ar); thus, the physicochemical characterization of the LMNO samples was conducted with samples obtained at 700 °C.

4.4. Electrochemical Characterization. The LMNO cathode laminate was fabricated by mixing a slurry containing 80% LMNO, 10% carbon black, and 10% poly(vinylidene fluoride) in *N*-methyl-2-pyrrolidone. The prepared mix was pasted on an aluminum current collector and vacuum-dried at 110 °C for 12 h. The dried laminate was then punched into 12 mm disc for coin-cell assembly and transferred into the glovebox. The cells were assembled in the glovebox using Li foil as an anode. Lithium hexafluorophosphate ($LiPF_6$) in ethylene carbonate, dimethyl carbonate, and diethyl carbonate, (volume ratio 1:1:1) electrolyte (1 M), and a microporous polypropylene Celgard H1612/16 μm separator were used. The coin cells remained in the glovebox overnight before they were taken out for electrochemical measurements (CV: 2−4.9 V and galvanometry discharge: 3.5−4.8 V) using the BioLogic system (BCS-8xx series) instrument.

■ ASSOCIATED CONTENT

Supporting Information

The Supporting Information is available free of charge at https://pubs.acs.org/doi/10.1021/acsomega.1c03656.

SAED, TEM images, TGA, Raman, Coulombic efficiency and cycling stability, and DFT-determined structure (PDF)

■ AUTHOR INFORMATION

Corresponding Author

Kenneth I. Ozoemena − *Molecular Sciences Institute, School of Chemistry, University of the Witwatersrand, Johannesburg 2050, South Africa;* orcid.org/0000-0001-7107-7003; Phone: +27 11 7176730; Email: kenneth.ozoemena@wits.ac.za

Authors

Aderemi B. Haruna − *Molecular Sciences Institute, School of Chemistry, University of the Witwatersrand, Johannesburg 2050, South Africa*

Patrick Mwonga − *Molecular Sciences Institute, School of Chemistry, University of the Witwatersrand, Johannesburg 2050, South Africa*

Dean Barrett − *Molecular Sciences Institute, School of Chemistry, University of the Witwatersrand, Johannesburg 2050, South Africa*

Cristiane B. Rodella − *Brazilian Synchrotron Light Laboratory (LNLS/Brazilian Center of Energy and Materials) (CNPEM), Campinas 13083-970 São Paulo, Brazil;* orcid.org/0000-0003-1683-4264

Roy P. Forbes − *Molecular Sciences Institute, School of Chemistry, University of the Witwatersrand, Johannesburg 2050, South Africa*

Andrew Venter − *Research and Technology Development Division, Necsa (South African Nuclear Energy Corporation) SOC Limited, Pretoria 0001, South Africa*

Zeldah Sentsho − *Research and Technology Development Division, Necsa (South African Nuclear Energy Corporation) SOC Limited, Pretoria 0001, South Africa*

Philip J. Fletcher − *Materials and Chemical Characterization Facility (MC²), University of Bath, Bath BA2 7AY, U.K.*

Frank Marken − *Materials and Chemical Characterization Facility (MC²), University of Bath, Bath BA2 7AY, U.K.; Department of Chemistry, University of Bath, Bath BA27AY, U.K.*

Complete contact information is available at: https://pubs.acs.org/10.1021/acsomega.1c03656

Notes

The authors declare no competing financial interest.

■ ACKNOWLEDGMENTS

The authors are grateful for financial supports by the National Research Foundation (NRF), Department of Science and Innovation (DSI), and University of the Witwatersrand (WITS) under the NRF/DSI/Wits SARChI Chair in Materials Electrochemistry and Energy Technologies (MEET) (grant UID no. 132739). A.B.H. is grateful to WITS for doctoral and Postdoctoral Research Fellowship awards. The authors are grateful to CNPEM-LNLS for XPD, DXAS beamlines, and XPS.

■ REFERENCES

(1) Lee, E.-S.; Nam, K.-W.; Hu, E.; Manthiram, A. Influence of Cation Ordering and Lattice Distortion on the Charge−Discharge Behavior of $LiMn_{1.5}Ni_{0.5}O_4$ Spinel between 5.0 and 2.0 V. *Chem. Mater.* **2012**, *24*, 3610−3620.

(2) Shin, D. W.; Bridges, C. A.; Huq, A.; Paranthaman, M. P.; Manthiram, A. Role of Cation Ordering and Surface Segregation in High-Voltage Spinel $LiMn_{1.5}Ni_{0.5-x}M_xO_4$ (M = Cr, Fe, and Ga) Cathodes for Lithium-Ion Batteries. *Chem. Mater.* **2012**, *24*, 3720−3731.
(3) Chemelewski, K. R.; Lee, E.-S.; Li, W.; Manthiram, A. Factors Influencing the Electrochemical Properties of High-Voltage Spinel Cathodes: Relative Impact of Morphology and Cation Ordering. *Chem. Mater.* **2013**, *25*, 2890−2897.
(4) Jafta, C. J.; Mathe, M. K.; Manyala, N.; Roos, W. D.; Ozoemena, K. I. Microwave-Assisted Synthesis of High-Voltage Nanostructured $LiMn_{1.5}Ni_{0.5}O_4$ Spinel: Tuning the Mn^{3+} Content and Electrochemical Performance. *ACS Appl. Mater. Interfaces* **2013**, *5*, 7592−7598.
(5) Duncan, H.; Hai, B.; Leskes, M.; Grey, C. P.; Chen, G. Relationships between Mn^{3+} Content, Structural Ordering, Phase Transformation, and Kinetic Properties in $LiNi_xMn_{2-x}O_4$ Cathode Materials. *Chem. Mater.* **2014**, *26*, 5374−5382.
(6) Moorhead-Rosenberg, Z.; Huq, A.; Goodenough, J. B.; Manthiram, A. Electronic and Electrochemical Properties of $Li_{1-x}Mn_{1.5}Ni_{0.5}O_4$ Spinel Cathodes As a Function of Lithium Content and Cation Ordering. *Chem. Mater.* **2015**, *27*, 6934−6945.
(7) Mao, J.; Dai, K.; Xuan, M.; Shao, G.; Qiao, R.; Yang, W.; Battaglia, V. S.; Liu, G. Effect of Chromium and Niobium Doping on the Morphology and Electrochemical Performance of High-Voltage Spinel $LiNi_{0.5}Mn_{1.5}O_4$ Cathode Material. *ACS Appl. Mater. Interfaces* **2016**, *8*, 9116−9124.
(8) Liu, G. Q.; Wen, L.; Liu, Y. M. Spinel $LiNi_{0.5}Mn_{1.5}O_4$ and its derivatives as cathodes for high-voltage Li-ion batteries. *J. Solid State Electrochem.* **2010**, *14*, 2191−2202.
(9) Liu, H.; Zhang, X.; He, X.; Senyshyn, A.; Wilken, A.; Zhou, D.; Fromm, O.; Niehoff, P.; Yan, B.; Li, J.; Muehlbauer, M.; Wang, J.; Schumacher, G.; Paillard, E.; Winter, M.; Li, J. Truncated Octahedral High-Voltage Spinel $LiNi_{0.5}Mn_{1.5}O_4$ Cathode Materials for Lithium Ion Batteries: Positive Influences of Ni/Mn Disordering and Oxygen Vacancies. *J. Electrochem. Soc.* **2018**, *165*, A1886−A1896.
(10) Lee, K.; Yang, G. J.; Kim, Y. Improvement of the electrochemical properties of $LiNi_{0.5}Mn_{1.5}O_4$ by controlling the heating atmosphere during synthesis. *Ceram. Int.* **2017**, *43*, 15510−15518.
(11) Liu, G.; Zhang, J.; Zhang, X.; Du, Y.; Zhang, K.; Li, G.; Yu, H.; Li, C.; Li, Z.; Sun, Q.; Wen, L. Study on oxygen deficiency in spinel LiNi0.5Mn1.5O4 and its Fe and Cr-doped compounds. *J. Alloys Compd.* **2017**, *725*, 580−586.
(12) Oh, G.; Hirayama, M.; Kwon, O.; Suzuki, K.; Kanno, R. Effect of surface modification and oxygen deficiency on intercalation property of lithium nickel manganese oxide in an all-solid-state battery. *Solid State Ionics* **2016**, *288*, 244−247.
(13) Wang, L.; Chen, D.; Wang, J.; Liu, G.; Wu, W.; Liang, G. Synthesis of LiNi0.5Mn1.5O4 cathode material with improved electrochemical performances through a modified solid-state method. *Powder Technol.* **2016**, *292*, 203−209.
(14) Xue, Y.; Wang, Z.; Zheng, L.; Yu, F.; Liu, B.; Zhang, Y.; Ke, K. Investigation on preparation and performance of spinel $LiNi_{0.5}Mn_{1.5}O_4$ with different microstructures for lithium-ion batteries. *Sci. Rep.* **2015**, *5*, 13299.
(15) Xiao, J.; Chen, X.; Sushko, P. V.; Sushko, M. L.; Kovarik, L.; Feng, J.; Deng, Z.; Zheng, J.; Graff, G. L.; Nie, Z.; Choi, D.; Liu, J.; Zhang, J.-G.; Whittingham, M. S. High-Performance $LiNi_{0.5}Mn_{1.5}O_4$ Spinel Controlled by Mn^{3+} Concentration and Site Disorder. *Adv. Mater.* **2012**, *24*, 2109−2116.
(16) Cheng, F.; Zhang, T.; Zhang, Y.; Du, J.; Han, X.; Chen, J. Enhancing Electrocatalytic Oxygen Reduction on MnO_2 with Vacancies. *Angew. Chem., Int. Ed.* **2013**, *52*, 2474−2477.
(17) Wu, Q.-H.; Liu, M.; Jaegermann, W. X-ray photoelectron spectroscopy of $La_{0.5}Sr_{0.5}MnO_3$. *Mater. Lett.* **2005**, *59*, 1980−1983.
(18) Li, J.-Y.; Lü, H.-Y.; Zhang, X.-H.; Xing, Y.-M.; Wang, G.; Guan, H.-Y.; Wu, X.-L. P2-type Na0.53MnO2 nanorods with superior rate capabilities as advanced cathode material for sodium ion batteries. *Chem. Eng. J.* **2017**, *316*, 499−505.
(19) Hou, J.; Li, Y.; Liu, L.; Ren, L.; Zhao, X. Effect of giant oxygen vacancy defects on the catalytic oxidation of OMS-2 nanorods. *J. Mater. Chem. A* **2013**, *1*, 6736−6741.
(20) Zhai, T.; Xie, S.; Yu, M.; Fang, P.; Liang, C.; Lu, X.; Tong, Y. Oxygen vacancies enhancing capacitive properties of MnO2 nanorods for wearable asymmetric supercapacitors. *Nano Energy* **2014**, *8*, 255−263.
(21) Feng, J.; Huang, Z.; Guo, C.; Chernova, N. A.; Upreti, S.; Whittingham, M. S. An Organic Coprecipitation Route to Synthesize High Voltage $LiNi_{0.5}Mn_{1.5}O_4$. *ACS Appl. Mater. Interfaces* **2013**, *5*, 10227−10232.
(22) Hai, B.; Shukla, A. K.; Duncan, H.; Chen, G. The effect of particle surface facets on the kinetic properties of $LiMn_{1.5}Ni_{0.5}O_4$ cathode materials. *J. Mater. Chem. A* **2013**, *1*, 759.
(23) Jin, Y.-C.; Duh, J.-G. Feasible Nonaqueous Route to Synthesize High-Voltage Spinel Cathode Material for Lithium Ion Battery. *RSC Adv.* **2015**, *5*, 6919−6924.
(24) Wang, J.-f.; Chen, D.; Wu, W.; Wang, L.; Liang, G.-c. Effects of Na^+ doping on crystalline structure and electrochemical performances of $LiNi_{0.5}Mn_{1.5}O_4$ cathode material. *Trans. Nonferrous Met. Soc. China* **2017**, *27*, 2239−2248.
(25) Cabana, J.; Casas-Cabanas, M.; Omenya, F. O.; Chernova, N. A.; Zeng, D.; Whittingham, M. S.; Grey, C. P. Composition-Structure Relationships in the Li-Ion Battery Electrode Material $LiNi_{0.5}Mn_{1.5}O_4$. *Chem. Mater.* **2012**, *24*, 2952−2964.
(26) Alcántara, R.; Jaraba, M.; Lavela, P.; Tirado, J. L.; Zhecheva, E.; Stoyanova, R. Changes in the Local Structure of LiMgyNi0.5-yMn1.5O4 Electrode Materials during Lithium Extraction. *Chem. Mater.* **2004**, *16*, 1573−1579.
(27) Nesbitt, H. W.; Banerjee, D. Interpretation of XPS Mn(2p) spectra of Mn oxyhydroxides and constraints on the mechanism of MnO2 precipitation. *Am. Mineral.* **1998**, *83*, 305−315.
(28) Liu, G.; Du, Y.; Liu, W.; Wen, L. Study on the action mechanism of doping transitional elements in spinel $LiNi_{0.5}Mn_{1.5}O_4$. *Electrochim. Acta* **2016**, *209*, 308−314.
(29) Fan, L.; Liu, P. F.; Yan, X.; Gu, L.; Yang, Z. Z.; Yang, H. G.; Qiu, S.; Yao, X. Atomically isolated nickel species anchored on graphitized carbon for efficient hydrogen evolution electrocatalysis. *Nat. Commun.* **2016**, *7*, 10667.
(30) Shih, Y.-J.; Huang, Y.-H.; Huang, C. P. Electrocatalytic ammonia oxidation over a nickel foam electrode: Role of Ni(OH)-2(s)-NiOOH(s) nanocatalys. *Electrochim. Acta* **2018**, *263*, 261−271.
(31) Zhao, E.; Wei, L.; Guo, Y.; Xu, Y.; Yan, W.; Sun, D.; Jin, Y. Rapid hydrothermal and post-calcination synthesis of well-shaped $LiNi_{0.5}Mn_{1.5}O_4$ cathode materials for lithium ion batteries. *J. Alloys Compd.* **2017**, *695*, 3393−3401.
(32) Kishi, K.; Ikeda, S. X-ray Photoelectron Spectra of Evaporated Nickel Exposed To O_2 And H_2O. *Chem. Lett.* **1972**, *1*, 245−248.
(33) Mancini, M.; Gabrielli, G.; Axmann, P.; Wohlfahrt-Mehrens, M. Electrochemical Performance and Phase Transitions between 1.5 and 4.9 V of Highly-Ordered $LiNi_{0.5}Mn_{1.5}O_4$ with Tailored Morphology: Influence of the Lithiation Method. *J. Electrochem. Soc.* **2017**, *164*, A6229−A6235.
(34) Nisar, U.; Al-Hail, S. A. J. A.; Petla, R. K.; Shakoor, R. A.; Essehli, R.; Kahraman, R.; AlQaradawi, S. Y.; Kim, D. K.; Belharouak, I.; Amin, M. R. Understanding the Origin of the Ultrahigh Rate Performance of a SiO2-Modified LiNi0.5Mn1.5O4 Cathode for Lithium-Ion Batteries. *ACS Appl. Energy Mater.* **2019**, *2*, 7263−7271.
(35) Wu, Q.; Zhang, X.; Sun, S.; Wan, N.; Pan, D.; Bai, Y.; Zhu, H.; Hu, Y.-S.; Dai, S. Improved electrochemical performance of spinel LiMn1.5Ni0.5O4 through MgF2 nano-coating. *Nanoscale* **2015**, *7*, 15609−15617.
(36) Wang, L.; Li, H.; Huang, X.; Baudrin, E. A comparative study of *Fd-m* and $P4_332$ $LiNi_{0.5}Mn_{1.5}O_4$. *Solid State Ionics* **2011**, *193*, 32−38.
(37) Kunduraci, M.; Al-Sharab, J. F.; Amatucci, G. G. High-Power Nanostructured $LiMn_{2-x}Ni_xO_4$ High-Voltage Lithium-Ion Battery

https://doi.org/10.1021/acsomega.1c03656
ACS Omega 2021, 6, 25562−25573

Electrode Materials: Electrochemical Impact of Electronic Conductivity and Morphology. *Chem. Mater.* **2006**, *18*, 3585−3592.
(38) Adekunle, A. S.; Ozoemena, K. I. Electron transfer behaviour of single-walled carbon nanotubes electro-decorated with nickel and nickel oxide layers. *Electrochim. Acta* **2008**, *53*, 5774−5782.
(39) Ozoemena, K. Anodic Oxidation and Amperometric Sensing of Hydrazine at a Glassy Carbon Electrode Modified with Cobalt (II) Phthalocyanine−cobalt (II) Tetraphenylporphyrin (CoPc- (CoTPP)-4) Supramolecular Complex. *Sensors* **2006**, *6*, 874−891.
(40) Ozoemena, K. I.; Mathebula, N. S.; Pillay, J.; Toschi, G.; Verschoor, J. A. Electron transfer dynamics across self-assembled N-(2-mercaptoethyl) octadecanamide/mycolic acid layers: impedimetric insights into the structural integrity and interaction with anti-mycolic acid antibodies. *Phys. Chem. Chem. Phys.* **2010**, *12*, 345−357.
(41) Reddy, M. V.; Andreea, L. Y. T.; Ling, A. Y.; Hwee, J. N. C.; Lin, C. A.; Admas, S.; Loh, K. P.; Mathe, M. K.; Ozoemena, K. I.; Chowdari, B. V. R. Effect of preparation temperature and cycling voltage range on molten salt method prepared SnO_2. *Electrochim. Acta* **2013**, *106*, 143−148.
(42) Reddy, M. V.; Jie, T. W.; Jafta, C. J.; Ozoemena, K. I.; Mathe, M. K.; Nair, A. S.; Peng, S. S.; Idris, M. S.; Balakrishna, G.; Ezema, F. I.; Chowdari, B. V. R. Studies on Bare and Mg-doped $LiCoO_2$ as a cathode material for Lithium ion Batteries. *Electrochim. Acta* **2014**, *128*, 192−197.
(43) Raju, K.; Ozoemena, K. I. Hierarchical one-dimensional ammonium nickel phosphate microrods for high-performance pseudocapacitors. *Sci. Rep.* **2015**, *5*, 17629.
(44) Dong, H.; Zhang, Y.; Zhang, S.; Tang, P.; Xiao, X.; Ma, M.; Zhang, H.; Yin, Y.; Wang, D.; Yang, S. Improved High Temperature Performance of a Spinel $LiNi_{0.5}Mn_{1.5}O_4$ Cathode for High-Voltage Lithium-Ion Batteries by Surface Modification of a Flexible Conductive Nanolayer. *ACS Omega* **2019**, *4*, 185−194.
(45) Edström, K.; Gustafsson, T.; Thomas, J. O. The cathode−electrolyte interface in the Li-ion battery. *Electrochim. Acta* **2004**, *50*, 397−403.
(46) Choi, W.; Shin, H.-C.; Kim, J. M.; Choi, J.-Y.; Yoon, W.-S. Modeling and Applications of Electrochemical Impedance Spectroscopy (EIS) for Lithium-ion Batteries. *J. Electrochem. Sci. Technol.* **2020**, *11*, 1−13.
(47) Sui, N.; Duan, Y.; Jiao, X.; Chen, D. Large-Scale Preparation and Catalytic Properties of One-Dimensional α/β-MnO_2 Nanostructures. *J. Phys. Chem. C* **2009**, *113*, 8560−8565.
(48) Yang, J.; Zhang, X.; Zhu, Z.; Cheng, F.; Chen, J. Ordered spinel $LiNi_{0.5}Mn_{1.5}O_4$ nanorods for high-rate lithium-ion batteries. *J. Electroanal. Chem.* **2013**, *688*, 113−117.
(49) Cheng, H.; Lu, C.; Liu, J.; Yan, Y.; Han, X.; Jin, H.; Wang, Y.; Liu, Y.; Wu, C. Synchrotron radiation X-ray powder diffraction techniques applied in hydrogen storage materials—A review. *Prog. Nat. Sci-Mater.* **2017**, *27*, 66−73.
(50) Venter, A. M.; van Heerden, P. R.; Marais, D.; Raaths, J. C.; Sentsho, Z. N. PITSI: The neutron powder diffractometer for transition in structure investigations at the SAFARI-1 research reactor. *Phys. Rev. B Condens. Matter* **2018**, *551*, 422−425.
(51) Ravel, B.; Newville, M. ATHENA, ARTEMIS, HEPHAESTUS: data analysis for X-ray absorption spectroscopy usingIFEFFIT. *J. Synchrotron Radiat.* **2005**, *12*, 537−541.

https://doi.org/10.1021/acsomega.1c03656
ACS Omega 2021, 6, 25562−25573